Catalysis Today 153 (2010) 118–124

Contents lists available at ScienceDirect

Catalysis Today

journal homepage: www.elsevier.com/locate/cattod

Simulation on catalytic reaction in diesel particulate filter

Kazuhiro Yamamoto*, Masamichi Nakamura, Hiroyoshi Yane, Hiroshi Yamashita

Department of Mechanical Science and Engineering, Nagoya University, Furo-cho, Chikusa-ku, Nagoya, Aichi 464-8603, Japan

ARTICLE INFO

Article history:
Available online 3 April 2010

Keywords:
Catalyst
DPF
Soot
Porous media
Computed tomography

ABSTRACT

To reduce particulate matters (PM) in diesel exhaust gas, stricter exhaust emission standards such as Euro V are being set in many countries. Recently, for the after-treatment of exhaust gas, a diesel particulate filter (DPF) has been developed. Latest researches have shown that DPF filtration efficiency can be as high as 99%. However, the filter would be plugged with particles to cause an increase of filter back-pressure, which must be kept at lower levels, because the higher back-pressure increases fuel consumption and reduces available torque. Here, we are focusing on NO_x-soot conversion system. There are two stages for PM oxidation. At the first step, the catalyst oxidizes NO in exhaust gas into NO_2. At the next step, NO_2 reacts with soot to produce CO and CO_2. However, the reaction rate and quantitative effect of NO_2 on soot oxidation is not clear, because it is difficult to observe small-scale phenomena in DPF experimentally, and there is not enough information on the PM oxidation. In this study, we simulated the above two-stage system. In the first part, the reaction with Pt catalyst for the oxidation of NO to NO_2 was simulated in non-porous flow-through filter. The catalytic reaction mechanism was discussed. In the second part, we simulated the flow in wall-flow filter to confirm the effectiveness of regeneration process by NO_2 in the real cordierite DPF.

1. Introduction

The pollution emitted by diesel cars such as heavy-duty trucks and buses causes environmental problems. The fine particles known as particulate matters (PM) can penetrate deep into the lungs and pose serious health risks including aggravated asthma, lung damage, and human carcinogen [1]. In many countries, stricter exhaust emission standards such as Euro V are being set. Then, the after-treatment of diesel exhaust gas is needed.

Recently, for the after-treatment of soot particles in exhaust gas, a diesel particulate filter (DPF) has been developed. One of the common types of DPF is a monolithic wall-flow filter. One example in Fig. 1 is a cordierite filter used in this study. PM is trapped when exhaust gas passes its porous wall (Fig. 1b). It is the most efficient after-treatment device. Latest researches have shown that DPF filtration efficiency can be as high as 99% [2–4]. However, the filter would be plugged with particles to cause an increase of filter back-pressure, which must be kept at lower levels, because the higher back-pressure increases fuel consumption and reduces available torque [5]. There are two methods, on-board and off-board regenerations. As for the off-board regeneration, the DPF is periodically replaced, or removed to eliminate hydrocarbons and particles by an electric heater. The system equipped with a temperature controller, compressed air source, and combustion devices is relatively large and complicated.

It is more appropriate to use the on-board regeneration, although it is still under development. It is passive regeneration, and its process is spontaneously conducted during the normal engine operation, which is called continuously regenerating trap (CRT). The filter surface is coated with noble metal catalysts such as platinum, mainly to reduce the temperature of soot oxidation [6]. So far, there are two approaches for on-board regeneration. One is to use a Ce-based fuel additive [7]. Its disadvantage is that, if the temperature is not sufficient, the presence of additive could prevent the direct soot oxidation by oxygen. Also, it should be substantially confirmed that the combustion products from Ce are not harmful to the environment.

We are focusing on NO_x-soot conversion system. The commercial DPF system such as Johnson Matthey CRT has been developed [8,9]. There are two stages for PM oxidation. At the first step, the catalyst oxidizes NO in exhaust gas into NO_2 in non-porous flow-through filter. At the next step, NO_2 reacts with soot to produce CO and CO_2 in wall-flow filter. It has been pointed out that NO_2 is much more reactive for soot oxidation [10–12]. So far, the reaction rate and quantitative effect of NO_2 on soot oxidation have not been clear. To confirm the applicability of the above system, we need to understand the phenomena in the real wall-flow filter. Typically, the inlet size of filter monolith is about 2 mm, and the thickness of the filter wall where soot particles are removed is only 0.2 mm. It is difficult to observe the small-scale phenomena inside the fil-

* Corresponding author. Fax: +81 52 789 4471.
E-mail address: kazuhiro@mech.nagoya-u.ac.jp (K. Yamamoto).

0920-5861/$ – see front matter © 2010 Elsevier B.V. All rights reserved.
doi:10.1016/j.cattod.2010.02.064

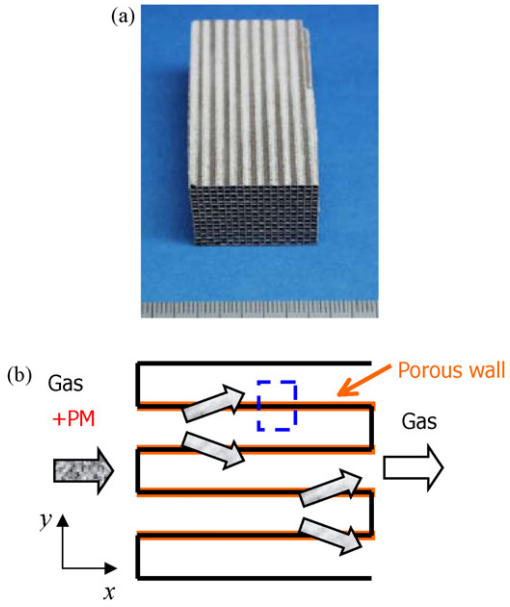

Fig. 1. (a) Photograph of cordierite DPF and (b) PM trap inside wall-flow filter. Calculation domain in Fig. 4 is roughly shown by dotted line.

ter experimentally, and there is not enough information on the PM oxidation with catalyst.

In this study, we simulated the flow in DPF by lattice Boltzmann method (LBM). The structure of the real cordierite filter was scanned by a 3D X-ray CT (Computed Tomography) technique. Non-destructive nature of the CT technique allows visualization of filter inner structure actually used. In our previous study [13–15], we have confirmed the applicability of the tomography-assisted simulation. In the present simulation, we employed a similar data processing technique. Figure 2 shows a CT image of the filter. The spatial resolution is 1 μm/pixel, which is the finest level in the reported CT measurements. Left figure shows the image area of the filter in x–y plane, and right figure shows digitized data used in simulation. Its total size is 400 μm(x) × 400 μm(y) × 200 μm(z). Complex porous structure with variety of pore size is well observed. Based on 3D CT data, it is found that the averaged porosity is about 0.4. By conducting tomography-assisted simulation, it is possible to discuss local velocity and pressure distributions in the real filter, which are hardly obtained by measurements.

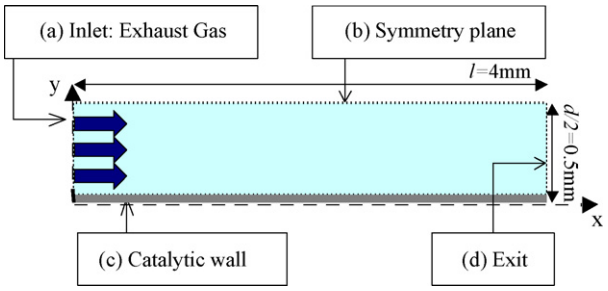

Fig. 3. Schematic of analytical model for non-porous flow-through filter.

2. Numerical method

In this study, two stages in the NO_x-soot conversion system were simulated separately. One is the catalytic oxidation of NO to NO_2, and the other is NO_2 reaction with soot to produce CO and CO_2. In this section, numerical models for these processes are explained, respectively.

2.1. Catalytic reaction

In the first process of NO oxidation in the flow-through filter, the detailed reaction scheme was used in the simulation. In the gas phase, the elementary reaction kinetics was considered. On the other hand, in the solid phase, the adsorption, desorption, and surface reaction on platinum catalysts were considered. Then, the details of NO_2 formation from NO on Pt can be discussed.

2.1.1. Analytical model

Figure 3 shows an analytical model of two-dimensional parallel channel for honeycomb catalyst, which is the non-porous flow-through filter. A Cartesian coordinate system is employed: x is in the principal flow direction, y is in the transverse direction. The origin is on the lower side of channel at the inlet. The width d and length l of channel are 1 mm and 4 mm, respectively. The upper side of channel is the boundary of a symmetry plane. The gas flows out freely at the exit. The lower side of channel is catalytic wall surface.

2.1.2. Governing equation of gas phase

The governing equations of gas phase are the overall continuity equation, the Navier–Stokes equation, the energy equation, and species continuity equation and the equation of state.

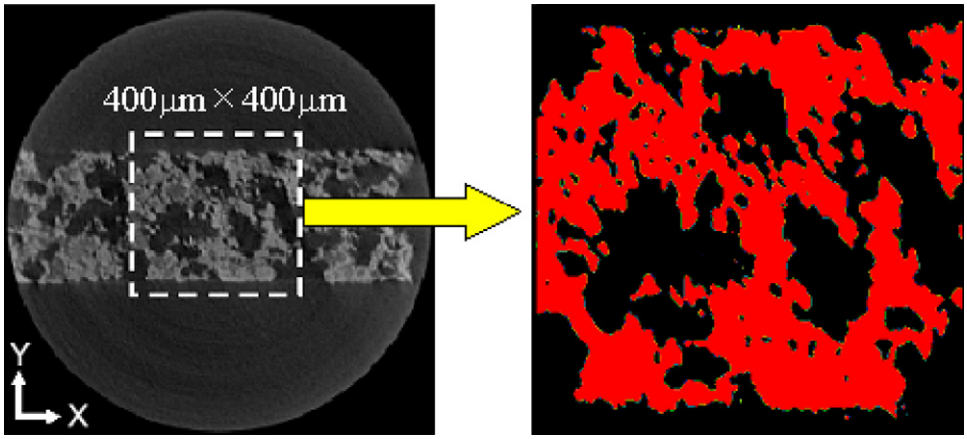

Fig. 2. Inner structure of DPF is obtained by X-ray CT technique. Left figure shows the image area of the filter in x–y plane, and right figure shows digitized data used in simulation.

$$\frac{\partial \rho}{\partial t} + \frac{\partial(\rho v_x)}{\partial x} + \frac{\partial(\rho v_y)}{\partial y} = 0 \tag{1}$$

$$\frac{\partial(\rho v_x)}{\partial t} + \frac{\partial(\rho v_x^2)}{\partial x} + \frac{\partial(\rho v_x v_y)}{\partial y} = -\frac{\partial p}{\partial x} + \frac{\partial}{\partial x}\left(\mu \frac{\partial v_x}{\partial x}\right) + \frac{\partial}{\partial y}\left(\mu \frac{\partial v_x}{\partial y}\right) \tag{2}$$

$$\frac{\partial(\rho v_y)}{\partial t} + \frac{\partial(\rho v_y^2)}{\partial y} + \frac{\partial(\rho v_x v_y)}{\partial x} = -\frac{\partial p}{\partial y} + \frac{\partial}{\partial x}\left(\mu \frac{\partial v_y}{\partial x}\right) + \frac{\partial}{\partial y}\left(\mu \frac{\partial v_y}{\partial y}\right) \tag{3}$$

$$\frac{\partial(\rho Y_i)}{\partial t} + \frac{\partial(\rho v_x Y_i)}{\partial x} + \frac{\partial(\rho v_y Y_i)}{\partial y} = \frac{\partial}{\partial x}\left(\rho D_i \frac{\partial Y_i}{\partial x}\right) + \frac{\partial}{\partial y}\left(\rho D_i \frac{\partial Y_i}{\partial y}\right) + w_i \tag{4}$$

$$c_p\left[\frac{\partial(\rho T)}{\partial t} + \frac{\partial(\rho v_x T)}{\partial x} + \frac{\partial(\rho v_y T)}{\partial y}\right] = \frac{\partial}{\partial x}\left(\lambda \frac{\partial T}{\partial x}\right) + \frac{\partial}{\partial y}\left(\lambda \frac{\partial T}{\partial y}\right) - \sum_{i=1}^{N_g} h_i w_i \tag{5}$$

$$p = \rho RT \sum_{i=1}^{N_g} \frac{Y_i}{m_i} \tag{6}$$

These governing equations were discretized using the finite volume method. The SIMPLE (Semi-Implicit Method for Pressure-Linked Equation) method proposed by Ptankar was used for the coupling of velocity and pressure fields [16,17]. Convective terms were computed by adopting the first-order up-wind scheme, and the full implicit Euler method was used for the time advance. The time step was 1 μs in the simulation.

As for the physical properties, the thermodynamic constants were taken to be temperature-dependent, and the species specific heats at constant pressure were approximated by a polynomial fit of the temperature to the JANNAF data [18]. Transport properties were calculated according to the simplified transport model proposed by Smooke [19]. GRI-mech.3.0 was applied to the chemical kinetic model in the gas phase, where 53 chemical species (N_g = 53) and 325 elementary reactions were considered [20].

As for boundary conditions, the inflow velocity and temperature are U_{in} = 1.0 m/s and T_{in} = 650 K at inlet, respectively. The mixture at inlet was assumed to be that in diesel exhaust gas with mass fraction $Y_i = Y_{i,in}$. Its composition consists of 500–1500 ppm NO, 500 ppm CO, 10 mol% O_2, 6 mol% CO_2, and 7 mol% H_2O, and the rest is N_2 [15,21].

$$v_x = U_{in} \tag{7}$$

$$T = T_{in} \tag{8}$$

The boundary conditions for the upper side of channel are as follows based on symmetry:

$$\frac{\partial F}{\partial y} = 0 \quad (F: v_x, Y_i, T) \tag{9}$$

$$v_y = 0 \tag{10}$$

The boundary conditions for the exit of channel are based on the developed boundary condition:

$$\frac{\partial F}{\partial x} = 0 \quad (F: v_x, v_y, Y_i, T) \tag{11}$$

2.1.3. Governing equation of solid phase

The governing equations of solid phase are the conservation equations of surface chemical species. These equations are expressed in terms of the time changes in the coverage of surface chemical species, which are controlled by catalytic reactions. The catalytic reactions consist of adsorption A(i), desorption D(i) and surface reaction R(j), where i is the chemical species in gas phase, and j is the number of elementary surface reaction. As for NO oxidation by platinum catalyst adopted in the present study, there are 6 surface species (O_2, NO, NO_2, CO, CO_2, and H_2O) and 18 elementary catalytic reactions in Eqs. (12)–(29), where the symbol(s) indicates the surface species, and Pt(s) indicates the catalytic site non-occupied with species. Eqs. (12)–(17) represent the adsorption, Eqs. (18)–(23) represent the desorption, and Eqs. (24)–(29) represent the surface reaction, respectively [22,23].

Adsorption

$$A(O_2): O_2 + 2Pt(s) \rightarrow 2O(s) \tag{12}$$

$$A(NO): NO + Pt(s) \rightarrow NO(s) \tag{13}$$

$$A(NO_2): NO_2 + Pt(s) \rightarrow NO_2(s) \tag{14}$$

$$A(CO): CO + Pt(s) \rightarrow CO(s) \tag{15}$$

$$A(CO_2): CO_2 + Pt(s) \rightarrow CO_2(s) \tag{16}$$

$$A(H_2O): H_2O + Pt(s) \rightarrow H_2O(s) \tag{17}$$

Desorption

$$D(O_2): 2O(S) \rightarrow O_2 + 2Pt(s) \tag{18}$$

$$D(NO): NO(S) \rightarrow NO + Pt(s) \tag{19}$$

$$D(NO_2): NO_2(S) \rightarrow NO_2 + Pt(s) \tag{20}$$

$$D(CO): CO(S) \rightarrow CO + Pt(s) \tag{21}$$

$$D(CO_2): CO_2(S) \rightarrow CO_2 + Pt(s) \tag{22}$$

$$D(H_2O): H_2O(S) \rightarrow H_2O + Pt(s) \tag{23}$$

Surface reaction

$$R(1): NO + O(s) \rightarrow NO_2(s) \tag{24}$$

$$R(2): NO_2(S) \rightarrow NO + O(s) \tag{25}$$

$$R(3): CO(s) + O(s) \rightarrow CO_2(s) + Pt(s) \tag{26}$$

$$R(4): CO_2(s) + Pt(s) \rightarrow CO(s) + O(s) \tag{27}$$

$$R(5): NO(s) + O(s) \rightarrow NO_2(s) + Pt(s) \tag{28}$$

$$R(6): NO_2(s) + Pt(s) \rightarrow NO(s) + O(s) \tag{29}$$

The adsorption rate of W_i^a, desorption rate of W_i^d, and surface reaction of W_j^r are expressed in Eqs. (30)–(32), respectively.

$$W_i^a = K_i^a S_i, \quad K_i^a = \frac{p_i}{\sqrt{2\pi m_i RT}} \cdot N_A \cdot A, \quad S_i = S_i^0\left(1 - \theta_{all}\right)^n \tag{30}$$

$$W_i^d = K_i^d \theta_{i'(s)}, \quad K_i^d = A_i \exp\left(-\frac{E_i^d - \alpha_i \theta_i}{RT_s}\right) \tag{31}$$

$$W_j^r = K_j^r \theta_{i(s)} \theta_{i'(s)}, \quad K_j^r = A_j \exp\left(-\frac{E_j - \alpha_j \theta_j}{RT_s}\right) \tag{32}$$

where N_A is the Avogadro constant, S_i is the sticking coefficient, A_i is the desorption constant, α_i and α_j are the constant, and θ_i is the

coverage for each species. The surface area per catalytic site of A is 4×10^{-20} m^2.

2.2. Soot oxidation

In the second process of soot oxidation, we considered the wall-flow filter. We obtained the porous structure of cordierite filter by a 3D X-ray CT technique. The simulation was conducted in 3D, and the lattice Boltzmann method (LBM) was used.

2.2.1. Lattice Boltzmann method (LBM)

The fundamental idea of the LBM is to construct simplified kinetic models that incorporate the essential physics of microscopic or mesoscopic processes so that the macroscopic averaged properties obey the desired macroscopic equations such as the *N–S* equation. It is well known that, due to easy implementation of boundary conditions, LBM is appropriate for the simulation of porous media flow [24]. The LBM fulfills these requirements in a straightforward manner.

Here, we explain the numerical procedure [13–15]. The flow is described by the lattice BGK equation in terms of the distribution function. The 3D LBGK model evolves on the lattice space with the following 15 discrete velocities.

$$[\,c_1 \;\; c_2 \;\; c_3 \;\; c_4 \;\; c_5 \;\; c_6 \;\; c_7 \;\; c_8 \;\; c_9 \;\; c_{10} \;\; c_{11} \;\; c_{12} \;\; c_{13} \;\; c_{14} \;\; c_{15}\,] = \begin{bmatrix} 1 & -1 & 0 & 0 & 0 & 0 & 1 & -1 & 1 & -1 & 1 & -1 & 1 & -1 & 0 \\ 0 & 0 & 1 & -1 & 0 & 0 & 1 & -1 & 1 & -1 & -1 & 1 & -1 & 1 & 0 \\ 0 & 0 & 0 & 0 & 1 & -1 & 1 & -1 & -1 & 1 & 1 & -1 & -1 & 1 & 0 \end{bmatrix} \quad (33)$$

where c is the advection speed. The evolution equation using the pressure distribution function is:

$$p_\alpha(x + c_\alpha \delta_t,\ t + \delta_t) - p_\alpha(x, t) = -\frac{1}{\tau}[p_\alpha(x, t) - p_\alpha^{eq}(x, t)] \quad (34)$$

where δ_t is the time step, and τ is the relaxation time that controls the rate of approach to equilibrium. The equilibrium distribution function, p_α^{eq}, is given by:

$$p_\alpha^{eq} = w_\alpha \left\{ p + p_0 \left[3\frac{(c_\alpha \cdot \boldsymbol{u})}{c^2} + \frac{9}{2}\frac{(c_\alpha \cdot \boldsymbol{u})^2}{c^4} - \frac{3}{2}\frac{\boldsymbol{u} \cdot \boldsymbol{u}}{c^2} \right] \right\} \quad (35)$$

where $w_\alpha = 1/9$ ($\alpha = 1{:}6$), $w_\alpha = 1/72$ ($\alpha = 7{:}14$), and $w_{15} = 2/9$. The sound speed, c_s, is $c/\sqrt{3}$ with $p_0 = \rho_0 R T_0 = \rho_0 c_s^2$. Here, p_0 and ρ_0 are the atmospheric pressure and density at the room temperature, respectively. In this study, to consider the variable density, we adopt the Mach number approximation. The pressure and local velocity of $\boldsymbol{v} = (v_x, v_y, v_z)$ are obtained using the ideal gas equation:

$$p = \sum_\alpha p_\alpha \quad (36)$$

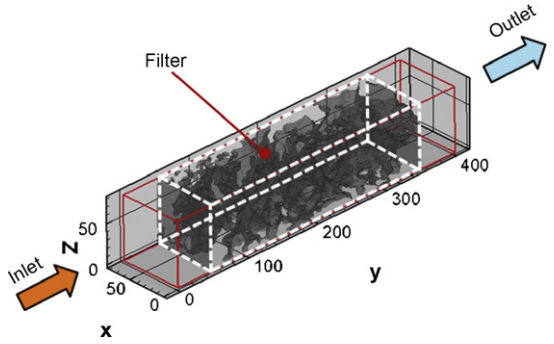

Fig. 4. Calculation domain and coordinate for wall-flow filter.

$$\boldsymbol{v} = \frac{\rho_0}{\rho}\frac{1}{p_0}\sum_\alpha c_\alpha p_\alpha \quad (37)$$

The relaxation time is related with transport coefficients, such as kinetic viscosity and diffusion coefficient using $\nu = (2\tau - 1)/6c^2\delta_t$. Then, through the Chapman–Enskog procedure, the Navier–Stokes equations are derived from these equations [24]. The LBM formula for temperature and concentration fields is:

$$F_{s,\alpha}(x + c_\alpha \delta_t,\ t + \delta_t) - F_{s,\alpha}(x, t) = -\frac{1}{\tau_s}[F_{s,\alpha}(x, t) - F_{s,\alpha}^{eq}(x, t)] + w_\alpha Q_s,$$
$$s = T, Y_i \quad (38)$$

where Q_s, is the source term due to chemical reaction. The equilibrium distribution function, $F_{s,\alpha}^{eq}$, is given by:

$$F_{s,\alpha}^{eq} = w_\alpha \cdot s \left\{ 1 + 3\frac{(c_\alpha \cdot \boldsymbol{u})}{c^2} + \frac{9}{2}\frac{(c_\alpha \cdot \boldsymbol{u})^2}{c^4} - \frac{3}{2}\frac{\boldsymbol{u}^2}{c^2} \right\} \quad (39)$$

The temperature, T, and mass fraction of species, Y_i, are determined by these distribution functions:

$$T = \sum_\alpha F_{T,\alpha} \quad (40)$$

$$Y_i = \sum_\alpha F_{Y_i,\alpha} \quad (41)$$

2.2.2. Analytical model

Figure 4 shows the calculation domain for wall-flow filter. As seen in Figs. 1b and 2, the direction of flow into the filter is x. Then, y is the direction across the filer wall, and z is the direction normal to x and y. The size is 80 μm(x) × 400 μm(y) × 80 μm(z), and the total number of grids is 81 × 401 × 81. The grid size is of 1 μm, which is the spatial resolution of the X-ray CT measurement. The filter is placed in the center part in this calculation domain. The inflow velocity, U_{in}, is 1 m/s, and the soot mass fraction at the inlet, $Y_{C,in}$, is 0.01. As for the boundary condition, the inflow boundary is adopted at the inlet. At the sidewall, the slip boundary condition is adopted, considering the symmetry. At the outlet, the pressure is constant (atmospheric pressure, p_{out}), and the gradient of species concentration and temperature is zero. On the surface of the filter or deposited soot layer, bounce-back rule for non-slip wall is adopted.

The reaction rate has been estimated based on previous experimental data [25]. The values of Arrhenius factor and activation energy are $A = 146$ 1/s, $E = 79.5$ kJ/mol with NO_2, and $A = 1.20$ 1/s, $E = 64.9$ kJ/mol without NO_2.

3. Results and discussion

3.1. Catalytic reaction and reaction route

First, NO and NO_2 concentrations in flow-through filter are examined to discuss the catalytic reaction. The distribution of NO_2 mass fraction is shown in Fig. 5 when NO mole fraction at the inlet is 1000 ppm. It is found that NO_2 mass fraction increases in the downstream. This indicates that NO_2 is formed on the catalytic wall, and is transported downstream. The profiles of NO_2 mass fraction in the cross-sections of $x = 1$ mm, 2 mm, 3 mm, and 4 mm are compared in

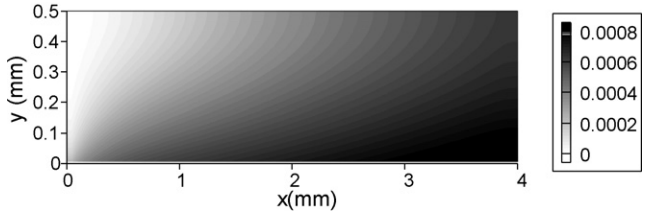

Fig. 5. NO_2 mass fraction in flow-through filter: U_{in} = 1.0 m/s; T_{in} = 650 K; $X_{NO,in}$ = 1000 ppm.

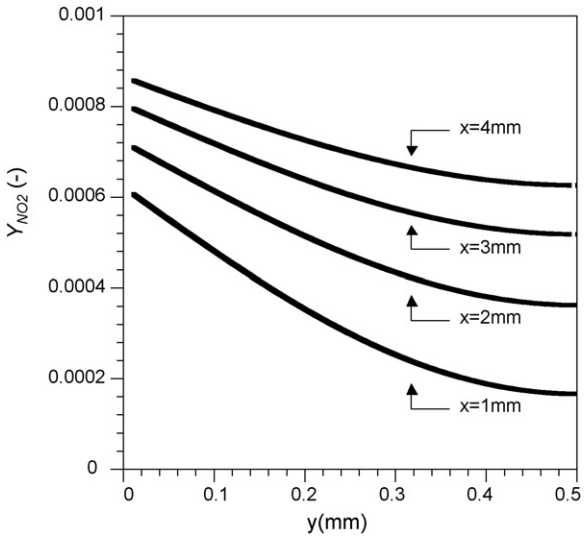

Fig. 6. Comparison of profiles of NO_2 mass fraction in cross-sections of x = 1 mm, 2 mm, 3 mm, and 4 mm in flow-through filter: U_{in} = 1.0 m/s; T_{in} = 650 K, $X_{NO,in}$ = 1000 ppm.

Fig. 6. Needless to say, NO_2 is formed on the catalytic surface, and NO_2 concentration is gradually increased along y-direction due to the diffusion.

The reaction route of NO oxidation by platinum catalyst is shown in Fig. 7. The route and magnitude of catalytic reaction rate are expressed by the direction and thickness of arrow. The gas phase species such as NO, O_2, CO, NO_2 and H_2O adsorb in or desorb from

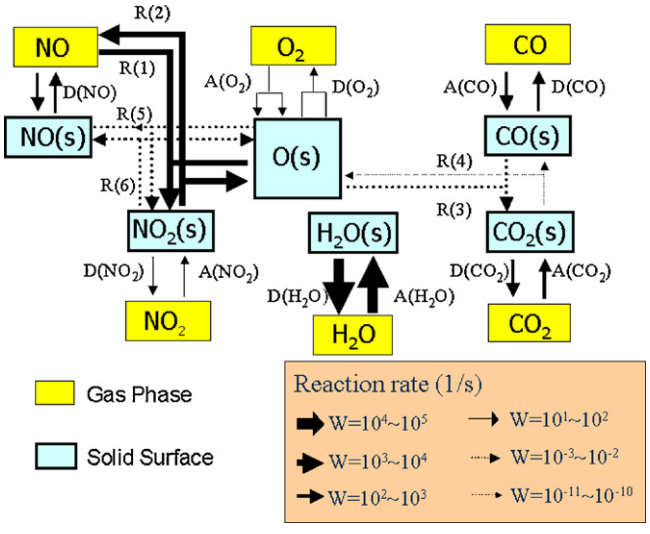

Fig. 7. Reaction route of NO oxidation is shown. The route and magnitude of catalytic reaction rate are expressed by direction and thickness of arrow. It is considered that gas phase species adsorb in or desorb from catalyst.

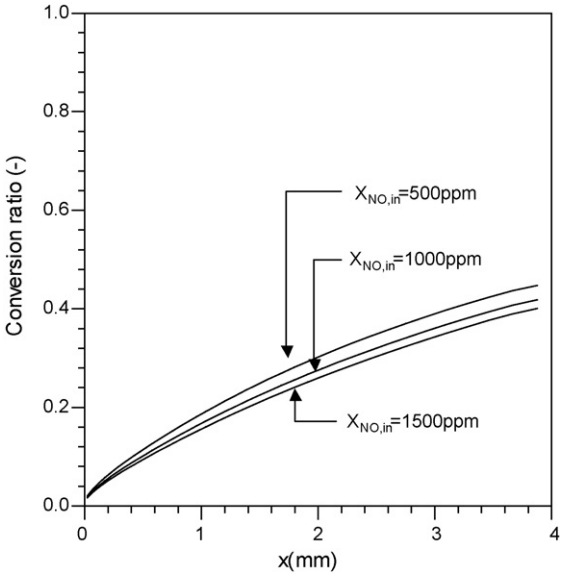

Fig. 8. Conversion ratio of NO_2 from NO is shown at different NO concentrations at the inlet: U_{in} = 1.0 m/s; T_{in} = 650 K; $X_{NO,in}$ = 500 ppm, 1000 ppm, and 1500 ppm.

catalyst. It should be noted that the reaction rates of R(3), R(4), R(5), and R(6) are very small. Thus, NO in the gas phase and O(s) adsorbed on the catalyst become NO_2(s) via the surface reaction of R(1). Then, NO_2(s) desorbs from catalyst and becomes NO_2 in the gas phase. The difference between the reaction rates of R(3) and R(4) is very small, and the difference between reaction rates of R(1) and R(2) is equal to that between the reaction rates of D(NO_2) and A(NO_2). It means that O(s) does not contribute the production of CO_2, but relates in the formation of NO_2. The reactions of A(H_2O) and D(H_2O) for the formation of H_2O are isolated from other reaction routes.

Here, the distribution of coverage θ_i for each species is examined. The coverage changes largely at the inlet, and is almost constant in the flow direction. The catalytic surface is almost occupied by O(s). The coverage of CO_2(s) is the smallest. Thus, the surface reaction R(1) between NO in the gas phase and O(s) adsorbed on the catalyst is the most important for the formation of NO_2.

Then, the effect of NO concentration is investigated. The mole fraction of $X_{NO,in}$ in the exhaust gas is changed from 500 to 1500 ppm. Expectedly, when NO concentration at the inlet is increased, NO_2 concentration at the exit is larger. Here, the conversion ratio of NO_2 from NO is defined as follows:

$$\eta_x = \frac{(1/M_{NO_2})\int_0^{d/2} \rho v_x Y_{NO_2} dy\Big|_{x=x}}{((1/M_{NO})\rho_{in} U_{in} Y_{NO,in})(d/2))} \quad (42)$$

where M_{NO} and M_{NO_2} are molecular weights of NO and NO_2, ρ is the density, and v_x is the velocity in the flow direction. The distribution of conversion ratio in the flow direction is shown in Fig. 8. The conversion ratio of NO_2 increases almost linearly in flow direction, showing that the amount of formation of NO_2 almost increases in proportion to the concentration of NO in the exhaust gas. At the exit, its value is about 0.4. Thus, NO_2 concentration can be increased, as the channel length is simply longer.

3.2. Flow and soot oxidation in DPF

Next, to see the velocity field inside wall-flow filter, we first simulated the flow without soot oxidation. Figure 9 shows the flow field inside the filter, which is under steady state with small velocity perturbation. The velocity vector is shown, with filter substrate by gray region. Three different slice images are shown at (a) y = 40 μm, (b)

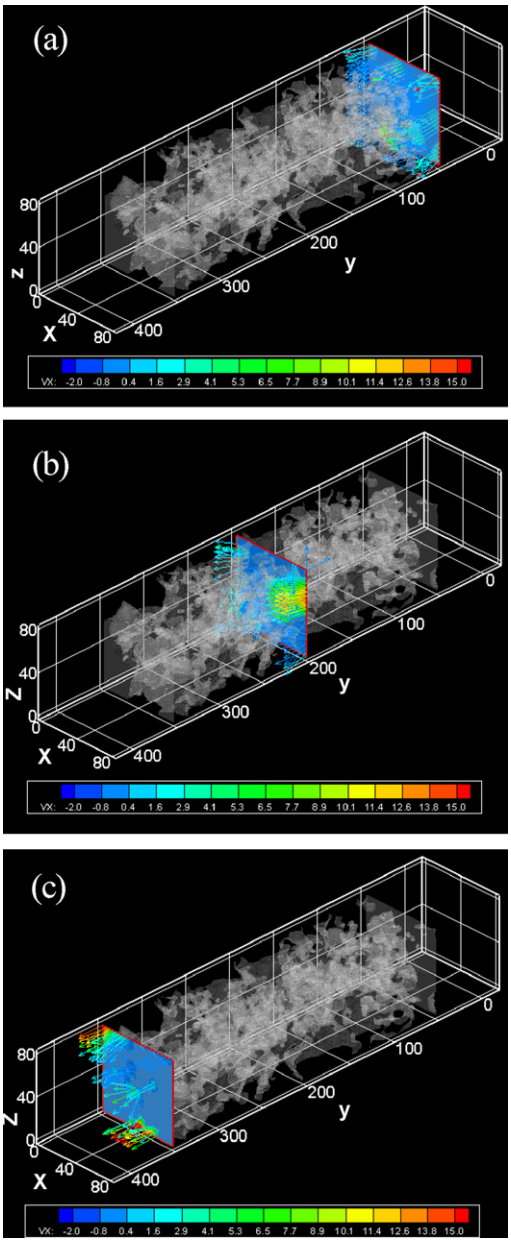

Fig. 9. Flow field in wall-flow filter is shown. Filter substrate is described by gray region: (a) $y = 40\ \mu m$, (b) $y = 190\ \mu m$, and (c) $y = 340\ \mu m$.

$y = 190\ \mu m$, and (c) $y = 340\ \mu m$. It should be noted that the cordierite filter has many small pores. Then, the velocity and its direction are largely changed when the flow passes through the filter wall.

We examined the pressure field along the flow direction (in y-axis), which is shown in Fig. 10. This pressure is the averaged value in x–z plane. For comparison, we checked the porosity distribution. The filter wall is located in the range of $50\ \mu m < y < 350\ \mu m$, and the porosity outside this region is unity. It is well known that, in case of homogenous porous media, the pressure linearly decreases along the flow direction, and the pressure gradient is constant [13,14]. However, as seen in this figure, since the porosity inside the filter wall is largely varied from 0.2 to 0.6, the pressure gradient is changed. In particular, at the filter inlet, the steep pressure gradient is observed, mainly due to the smaller porosity. Therefore, depending on the non-uniformity of pore structure, both flow and pressure are largely changed inside the wall-flow filter.

Finally, the soot oxidation was simulated for the filter regeneration process. Since it took more time to simulate the combustion

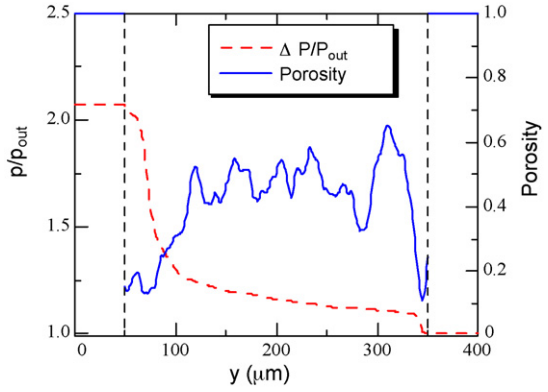

Fig. 10. Distributions of pressure and porosity across filter wall.

field, smaller calculation domain was used. The area is of $20\ \mu m < x < 60\ \mu m$ and $20\ \mu m < z < 60\ \mu m$ in Fig. 4. The oxygen concentration is 10% in the inflow gas, and the temperature is 650 K. To initiate the soot reaction, the temperature of both filter region and deposited soot layer is increased to 1200 K. Although the temperature of 1200 K may be too high in the passive regeneration, it could be possible in the active regeneration using excess fuel injection. The time, t, is counted after we set this temperature. For the initial soot distribution, the accumulated soot in DPF was 1.14 g/l.

Figure 11 shows the distributions in x–y plane of (a) filter region and deposited soot layer, (b) mass flux in y-direction, (c) pressure, and (d) temperature at $t = 4$ ms. These are the results with the reaction rate under NO_2 coexistence. In Fig. 11a, the light blue region is the filter substrate, and red region is the deposited soot layer. The velocity vector is also shown. The large pressure drop is observed in the deposited soot layer. The flow is accelerated due to the temperature rise. Since the heat release occurs due to soot combustion, the maximum temperature is higher than the initial soot layer temperature by 90 K.

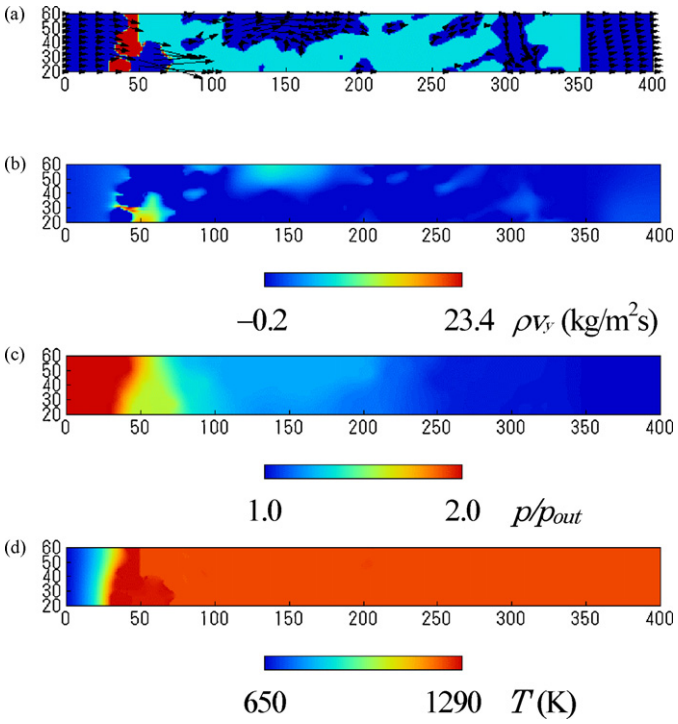

Fig. 11. Combustion field in x–y plane of (a) filter region and deposited soot layer with velocity vector, (b) mass flux in y-direction, (c) pressure, and (d) temperature: $t = 4$ ms.

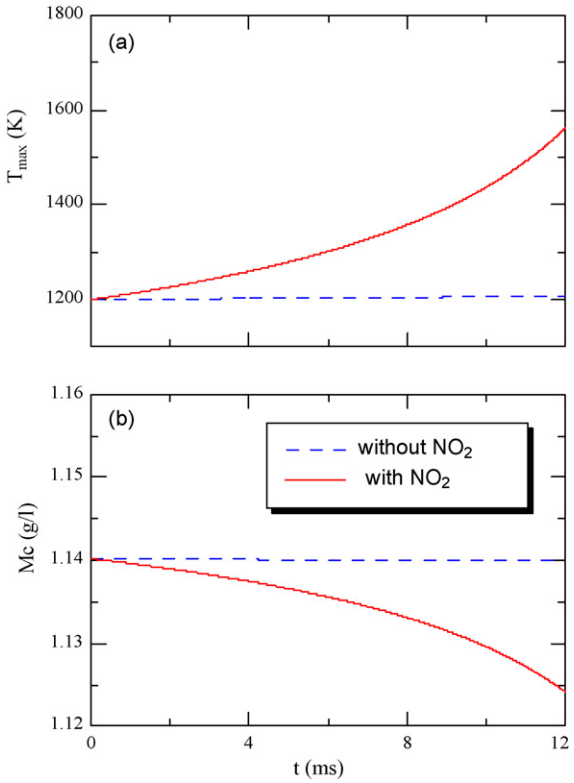

Fig. 12. (a) Maximum temperature of reaction region on the surface of soot layer and (b) mass of remained soot in DPF to observe effect of NO_2 on soot oxidation.

To evaluate the effect of NO_2 on the soot oxidation, two simulations were conducted using the reaction rates with and without NO_2. Figure 12a shows the maximum temperature of reaction region on the surface of soot layer. For comparison, the mass of remained soot in DPF is shown in Fig. 12b. Since the reaction is very slow without NO_2, the temperature change is very small in this period, and most of soot is not reacted. In contrast, under NO_2 coexistence, the large temperature increase is observed. Resultantly, more soot is oxidized. From this comparison, it is clear that the soot oxidation is largely accelerated in the flow with NO_2, and the effectiveness of regeneration process by NO_2 is confirmed in the simulation of real wall-flow DPF system.

4. Conclusions

We have simulated the flow in DPF to examine the catalytic reaction and soot oxidation for filter regeneration process. Inner structure of the cordierite filter was obtained by a 3D X-ray CT technique. Especially, the effect of NO_2 on the soot oxidation was evaluated. The following results are obtained.

(a) In the flow-through filter with Pt catalyst, the catalyst surface is almost occupied by O(s). The surface reaction between NO in the gas phase and O(s) adsorbed on the catalyst is the most important for the formation of NO_2.
(b) The conversion ratio of NO_2 from NO increases almost linearly in the flow direction. The amount of formation of NO_2 increases in proportion to the concentration of NO in the exhaust gas.
(c) The complex flow pattern is well visualized inside the wall-flow filter. The pressure distribution depends on the non-uniformity of pore structure.
(d) In combustion simulation, the filter regeneration process is well observed. When NO_2 is added, the soot oxidation is promoted to burn more soot in the filter. The effectiveness of regeneration process by NO_2 is confirmed in the real DPF system.

These are useful information to develop future NO_x-soot regenerating DPF system in the after-treatment of exhaust gas.

Acknowledgement

This work was partially supported by New Energy and Industrial Technology Development Organization in Japan (Industrial Technology Research Grant, 05A18020d).

References

[1] United States Environmental Protection Agency, Technical Highlights, EPA420-F03-017, 2003, p. 1.
[2] J.C. Clerc, Applied Catalysis B 10 (1996) 99.
[3] A.G. Konstandopoulos, M. Kostoglou, E. Skaperdas, E. Papaioannou, D. Zarvalis, E. Kladopoulou, SAE Technical Paper 2000-01-1016, 2000.
[4] E. Wirojsakunchai, E. Schroeder, C. Kolodziej, D.E. Foster, N. Schmidt, T. Root, T. Kawai, T. Suga, T. Nevius, T. Kusaka, SAE Technical Paper 2007-01-0320, 2007.
[5] A.M. Stamatelos, Energy Conversion and Management 38 (1) (1997) 83.
[6] S. Wang, B. Haynes, Catalysis Communications 4 (2003) 591.
[7] G.C. Koltsakis, A.M. Stamatelos, AIChE Journal 42 (6) (1996) 1662.
[8] B.J. Cooper, H.J. Jung, J.E. Toss, US Patent, 4,902,487(1990).
[9] P. Hawker, Diesel emission control technology, Platinum Metals Review 39 (1995) 2.
[10] H.J. Stein, Applied Catalysis B 10 (1996) 69.
[11] G. Neri, L. Bonaccorsi, A. Donato, C. Milone, M.G. Musolino, A.M. Visco, Applied Catalysis B 11 (1997) 217.
[12] J. Oi-Uchisawa, A. Obuchi, A. Ogata, R. Enomoto, S. Kushiyama, Applied Catalysis B 21 (1999) 9.
[13] K. Yamamoto, N. Takada, M. Misawa, Proceedings of the Combustion Institute 30 (2005) 1509.
[14] K. Yamamoto, S. Satake, H. Yamashita, N. Takada, M. Misawa, Mathematics and Computers in Simulation 72 (2006) 257.
[15] K. Yamamoto, S. Satake, H. Yamashita, N. Takada, M. Misawa, International Journal of Modern Physics C 18 (4) (2007) 528.
[16] S.V. Ptanker, Numerical Heat Transfer and Fluid Flow, Mcgraw-Hill, 1980.
[17] H. Yamashita, JSME International Journal Series B 43 (2000) 97.
[18] R.J. Kee, F.M. Ruply, J.A. Miller, CHEMKIN-II: A Fortran Chemical Kinetics Package for the Analysis of Gas-Phase Chemical Kinetics, SAND89-8009, 1989.
[19] M.D. Smooke, Reduced Kinetic Mechanisms and Asymptotic Approximations for Methane-Air Flames, 1991, p. 1.
[20] GRI-mech 3.0, http://www.me.berkeley.edu/gri-mech.
[21] J. Oi-Uchisawa, A. Obuchi, Applied Catalysis B: Environmental 21 (1999) 9.
[22] V.P. Zhdanov, B. Kasemo, Surface Science Reports 29 (1997) 31.
[23] M. Crocoll, S. Kureti, Journal of catalysis 229 (2005) 480.
[24] S. Chen, G.D. Doolen, Annual Review of Fluid Mechanics 30 (1998) 329.
[25] K. Yamamoto, S. Satake, H. Yamashita, A. Obuchi, J. Oi-Uchisawa, Journal of Thermal Science and Technology 2 (2) (2009) 245.